PCCP

CrossMark
← click for updates

TiO₂ hierarchical sub-wavelength microspheres for high efficiency dye-sensitized solar cells

Jiang Sheng,[a] Linhua Hu,[b] Li'e Mo,[b] Jichun Ye*[a] and Songyuan Dai*[c]

Monodisperse anatase hierarchical microspheres were produced *via* a simple sol–gel process. These microspheres in the sub-wavelength diameter of 320–750 nm could scatter visible light efficiently as whispering gallery modes (WGM) corresponding to the dye sensitized wavelength, and load a large number of dye molecules with a large surface area (149.82 m² g⁻¹). Dye-sensitized solar cells (DSCs) based on the microsphere monolayer adsorbed light fully over the entire wavelength region and facilitated electrolyte diffusion due to larger voids between the microspheres, compared to the conventional film. Furthermore, the dynamics of electron transport and recombination was investigated systematically, indicating the higher charge collection efficiency of the TiO₂ microsphere film. Overall, DSCs based on the 7.5 μm hierarchical microsphere monolayer exhibited more outstanding photovoltaic performances, yielding a high power conversion efficiency (PCE) of 11.43% under simulated AM 1.5 sunlight. Half of the normal film thickness was used to cut the device cost significantly.

1. Introduction

Mesoporous films composed of TiO₂ nanoparticles with a high surface area for adsorbing a large number of dye molecules and with tuneable continuous pores for electrolyte transport have been assembled into dye-sensitized solar cells (DSCs), resulting in a PCE of 12% in recent years.[1] The semiconductor TiO₂ plays an important role in dye adsorption, separation and transportation of photo-generated carrier charges in DSCs. In order to achieve high efficiency, appropriate film morphologies and textures it is necessary to control the crystallinity, porosity and composition. Three TiO₂ crystalline forms including rutile,[2,3] anatase[2,4] and brookite[5] have been extensively used for investigation of DSCs, and it was found that the anatase structure exhibits remarkably excellent electrochemistry. The film microstructures, for example, one dimensional structures,[6–10] inverse opal structures,[11,12] and blocking layers,[13,14] are also attractive for promoting the charge collection efficiency.

A typical photoelectrode structure of the double-layer includes a *ca.* 10 μm dye loading layer (around 20 nm anatase particles) and a *ca.* 4 μm light-scattering layer (300–500 nm particles).
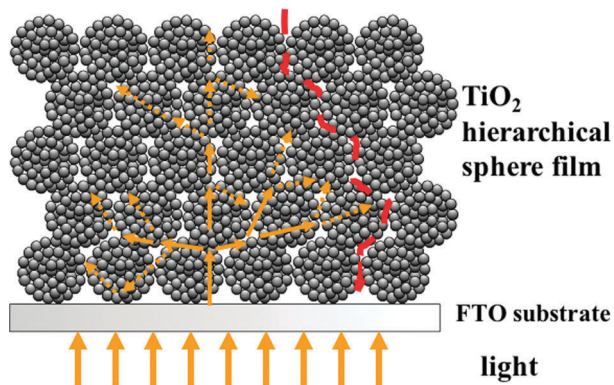
Since Rayleigh scattering caused by small nanoparticles is too weak to scatter the visible light,[15] the light is directly transported through the small size particle film until it is reflected backward by the large particles, leading to a short optical path in the films. Additionally, this scattering layer loads a few dye molecules due to its small surface area. Therefore, it is highly desirable to develop a bifunctional film to scatter visible light effectively and also have a large surface area for dye molecule adsorption. Furthermore, Chen[16,17] introduced previously the mesoporous TiO₂ microspheres into DSCs to improve the film structure. Dai developed the structures of microspheres by the Au plasma[18] and modified the synthesis process[19,20] to improve the PCE of DSCs. Herein, we have developed a close-packed bifunctional film composed of anatase hierarchical microspheres with appropriate diameter distribution. This structure reveals the improved visible light scattering and dye adsorption properties.

In this paper, TiO₂ hierarchical microspheres were prepared by a simple sol–gel method using ethanol and potassium chloride to control the hydrolysis and condensation reaction of titanium tetraisopropoxide, and their high crystalline frameworks were formed by hydrothermal treatment. Firstly, the monodisperse amorphous spheres with a diameter of 400–550 nm were prepared by the hydrolysis of a titanate precursor. After hydrothermal treatment with different ammonia concentrations, the hierarchical microspheres were formed by anatase nanoparticles with different sizes, and the diameter of microspheres ranged from 320 nm to 750 nm. Compared to the nanoparticle film, the TiO₂ hierarchical microsphere monolayer exhibited much more excellent optical characteristics, in which the light was

[a] *Ningbo Institute of Materials Technology and Engineering, Chinese Academy of Sciences, 1219 Zhongguan Road, Zhenhai, Ningbo, Zhejiang 315201, People's Republic of China. E-mail: jichun.ye@nimte.ac.cn*

[b] *Key Lab of Novel Thin Film Solar Cells, Institute of Applied Technology, Chinese Academy of Sciences, P.O. Box 1126, Hefei, Anhui 230031, People's Republic of China*

[c] *School of Renewable Energy, North China Electric Power University, 2 Beinong Road, Zhuxinzhuang, Changping, Beijing 102206, People's Republic of China. E-mail: sydai@ncepu.edu.cn*

This journal is © the Owner Societies 2016

Phys. Chem. Chem. Phys., 2016, **18**, 32293–32301 | **32293**

Scheme 1 Diagram of the light multiple diffractions and reflections (yellow line) and the electrolyte diffusion (red line) in the TiO_2 hierarchical microsphere monolayer.

scattered many times to extend the optical path until it was adsorbed absolutely (Scheme 1). The films also had a large surface area (149.82 m^2 g^{-1}) for dye adsorption and exhibited the interstitial voids for easy electrolyte diffusion. Based on this excellent monolayer, DSCs exhibited a high photovoltaic performance, with a PCE of 11.43%. The electron transport and recombination properties of the DSCs were also investigated systematically by IMPS, IMVS and EIS.

2. Experimental

2.1 Materials and reagents

Titanium tetraisopropoxide, LiI, I_2, 4-*tert*-butylpyridine (TBP), and acetonitrile (AN) were purchased from Sigma Aldrich. Ethanol, KCl, titanium tetrachloride ($TiCl_4$), ammonia (25%), triethyl-amine, ethyl cellulose and terpineol were obtained from Sinopharm Chemical Reagent Co. Ltd, China. 1,2-Dimethyl-3-*n*-propylimidazolium iodide (DMPII) was synthesized from 1,2-dimethylimidazole and propyl iodide purchased from Sigma Aldrich. Conducting glass (F-doped SnO_2, 15 Ω $\square^{-1}$ resistances and 90% transmittance) was obtained from Libbey-Owens-Ford Co., USA. The dye was N719 and C106, respectively.[21] The electrolyte was composed of 0.5 M LiI, 0.1 M I_2, 0.6 M tetrabutylammonium iodide, and 0.5 M tertbutylpyridine in acetonitrile.

2.2 Synthesis of TiO_2 hierarchical microspheres

A typical synthesis of amorphous TiO_2 microspheres was performed as follows.[16,22] A 200 ml ethanol solution was mixed with 0.8 ml of KCl (0.1 M) aqueous solution, dropwise adding 4 ml of titanium tetraisopropoxide at ambient temperature under a N_2 gas atmosphere under vigorous stirring for 10 min. The mixture solution was reacted statically for 3 h and a white precipitate was collected using a Millipore filter followed by washing with ethanol several times. Hydrothermal treatment was carried out in order to obtain TiO_2 hierarchical nanoporous spheres with a high crystalline framework. 2 g of the white amorphous precipitates were dispersed in a mixture solution of 60 ml ethanol and 30 ml distilled water, and then different

amounts of ammonia were added (0.0, 0.4 and 0.8 ml ammonia for samples S1, S2 and S3, respectively) under vigorous stirring. After stirring for 30 min the mixtures were placed in a Teflon-lined autoclave and treated at 160 °C for 20 h. The final products were collected by filtration and washed with ethanol and distilled water several times, respectively. The resultant powders were dispersed in ethanol for paste preparation.

2.3 Synthesis of TiO_2 nanoparticles

TiO_2 nanoparticles (NP) were prepared by the typical sol–gel procedure.[23] Titanium tetraisopropoxide (30 ml) was rapidly added to distilled water (60 ml) under vigorous stirring and then stirred for 30 min. A white precipitate formed immediately after addition of titanium tetraisopropoxide. The colloid was filtered and washed with distilled water and ethanol, and then placed in a closed vessel containing 30 ml of 0.6 M triethylamine aqueous solution and stirred at 90 °C until the slurry became a translucent blue-white liquid. The solution was moved to a Teflon-lined autoclave and treated hydrothermally at 220 °C for 5 h. After growth, the anatase nanoparticles were formed. The final powders were collected by centrifugation and washed with ethanol and distilled water several times, respectively.

2.4 Fabrication of DSCs

A series of pastes containing TiO_2 hierarchical spheres and nanoparticles were prepared as shown in our previous work.[6] Ethyl cellulose (15.0 g) and terpineol (15.0 g) were added into the ethanol suspension including 3.0 g TiO_2. The ethanol in solution was then removed by rotary evaporation to form viscous pastes. The colloidal paste was coated on conducting glass substrates[24] by screen-printing. The films (0.25 cm^2) were dried at room temperature for 10 min, and then sintered at 450 °C for 30 min in air, which were about 7.5 ± 0.3 μm thick. For obtaining a high performance, the freshly sintered films were immersed in the $TiCl_4$ (0.05 M) aqueous solution and placed in a closed vessel at 60 °C for 30 min. After washing with ethanol, the films were sintered again at 450 °C for 30 min. After cooling to 120 °C, these films were immersed in the dye solution for the whole night. The dye-loaded working electrode was assembled with a Pt-sputtered counter electrode and electrolyte by a 60 μm thermal adhesive film (Surlyn, Dupont). The DSCs fabricated from samples S1, S2, S3 and anatase nanoparticles were labeled as DSC-S1, DSC-S2, DSC-S3 and DSC-NPs.

2.5 Characterization

Morphologies of the samples were observed using a field emission scanning electron microscope (FE-SEM, Sirion 200, FEI Corp, Holland) and a transmission electron miscroscope (TEM, JEOL-2010, Japan). The crystallinity of TiO_2 hierarchical microspheres was characterized by X-ray powder diffraction (XRD, TTRAX3, CuKα/1.54 Å radiation, Rigaku, Japan). BET surface areas and the pore size of the sample powders were characterized using a BELSORP surface area analyzer. Diffused reflectance and transmittance spectra were recorded using a UV-vis spectrophotometer (U-3900H, Hitachi, Japan). The thicknesses of the films were measured using a surface profilometer

32294 | *Phys. Chem. Chem. Phys.*, 2016, **18**, 32293–32301

This journal is © the Owner Societies 2016

(XP-2, AMBIOS Technology Inc., USA). In order to analyze the surface concentration of the adsorbed dye in the films, the dye-loaded films were immersed in 0.1 M NaOH solution to desorb the dye, and then the absorption spectra of the desorbed-dye solution were recorded using a UV-vis spectrophotometer. The current density–voltage (J–V) characteristics of the solar cells were recorded using a Keithley 2400 digital source meter (Keithley, USA) under simulated sunlight (100 mW cm^{-2}) illumination provided by a xenon lamp (Oriel, USA) with an AM 1.5 filter. The incident monochromatic photon-to-current conversion efficiency (IPCE) was measured on the basis of the QE/IPCE Measurement Kit (Newport, USA). The electrochemical impedance spectra (EIS) were recorded using a computer controlled potentiostat (IM6ex, Zahner, Germany) in the frequency region from 20 mHz to 1000 kHz. The electron transport and recombination properties were measured by intensity-modulated photocurrent/photovoltage spectroscopy (IMPS/IMVS). For these measurements, a potentiostat controlled by a computer supplied the bias potential (IM6ex, Zahner, Germany) and light emitting diodes (Expot, Zahner, Germany) supplied the modulated light.

3. Results and discussion

The monodisperse amorphous microspheres were prepared by a sol–gel process, during which the concentrations of all reactants influenced the size distribution. Fig. 1 shows FE-SEM images of the as-prepared precursor and TiO$_2$ hierarchical microspheres after hydrothermal treatment with different ammonia concentrations. The precursors were monodisperse submicron spheres with a diameter of 400–550 nm, displaying a rather smooth surface and a firm body without crystalline features (Fig. 1a and b). The amorphous spheres were treated in a mixture of ethanol and water with different amounts of ammonia at 160 °C for 20 h in order to get the TiO$_2$ hierarchical porous spheres with a high surface area. After hydrothermal reaction, samples retained their spherical shape. Cheng[16] and Yang[25] previously reported that the size of spheres would shrunk to some extent. But in our experiment we found the growth of microspheres in the solution corresponding to the Ostwald ripening model. The big spheres grew larger from 550 nm to 750 nm in diameter, while small ones shrunk from 400 nm to 320 nm (Fig. 1c–h). Furthermore, a few spheres broke up into irregular clusters or nanoparticles in the solution with a high ammonia concentration. The wide diameter distribution of spheres was beneficial to expand the wavelength scope of scattering light. The spheres of the S1 sample were composed of the nanoparticles which were 11.7 ± 0.5 nm in diameter and compacted together observed over the surface of the spheres (Fig. 1c). The porous spheres of samples S2 and S3 treated in the mixture solution with ammonia had similar diameter distribution to sample S1. However, an increase in the nanoparticle size and a change in the morphology were observed in the presence of ammonia. The porous spheres of samples S2 and S3 were consisted of elongated nanoparticles with an average size of 16.0 ± 1.0 nm and 21.5 ± 0.5 nm in
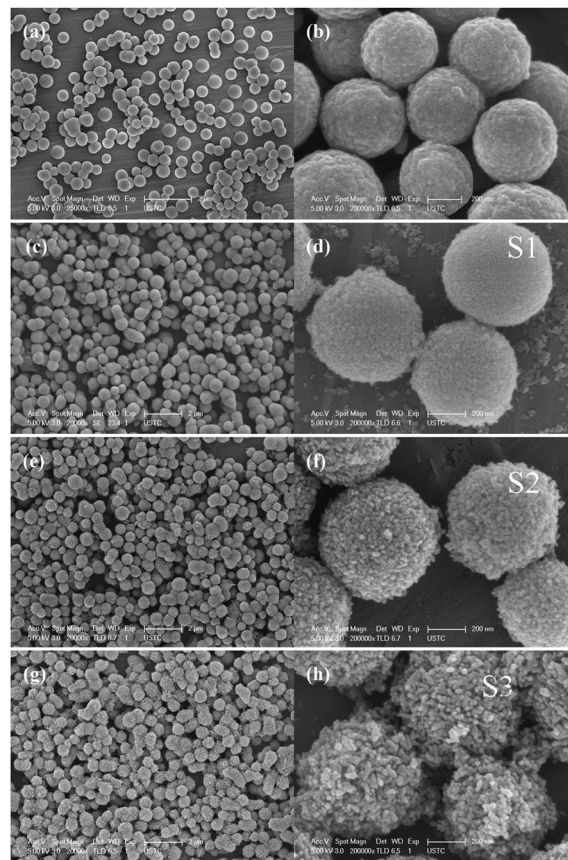

Fig. 1 FE-SEM images of the as-prepared spherical precursor (a and b), TiO$_2$ hierarchical microspheres after the hydrothermal treatment with different amounts of ammonia: sample S1 without ammonia (c and d); sample S2 with 0.4 ml ammonia (e and f) and sample S3 with 0.8 ml ammonia (g and h).

width and 39.2 ± 2.0 nm and 55.0 ± 3.0 nm in length, respectively. Upon increasing the ammonia concentration in the hydrothermal process, the size of the nanoparticles increased and the pore of the spheres enlarged from 7.28 nm to 12.39 nm. But the specific surface area decreased from 149.82 m^2 g^{-1} of S1 to 87.45 m^2 g^{-1} of S3 (Table 1). In the nanoparticle coarsening process, the solutions with ammonia were alkaline to ensure the TiO$_2$ crystal to be anatase without other phases. With increasing ammonia concentration, the Ti solubility increased to promote the TiO$_2$ redissolution from the amorphous phase and the nanoparticles grew larger, leaving lots of nanopores, even some small microspheres cracked into nanoparticles. Primarily due to Ostwald ripening, the anatase

Table 1 Physical properties of the TiO$_2$ hierarchical spheres (S1, S2 and S3) and nanoparticles

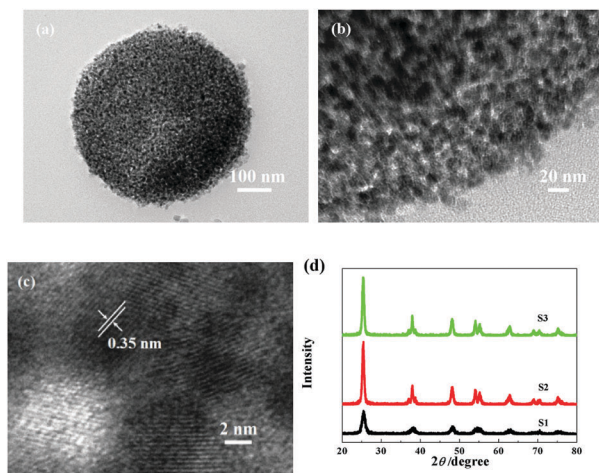| Samples	BET surface area (m^2 g^{-1})	Pore size (nm)	Porosity (%)	Dye amount (mol g^{-1})
S1	149.82	7.28	63.25	1.18 × 10^{-4}
S2	92.53	9.30	66.31	7.67 × 10^{-5}
S3	87.45	12.39	64.17	7.21 × 10^{-5}
NP	74.66	19.24	66.23	6.84 × 10^{-5}

Fig. 2 (a and b) TEM images of TiO$_2$ hierarchical microspheres, (c) HRTEM image of the nanoparticles with a high crystalline structure in the microsphere, (d) XRD patterns of the TiO$_2$ hierarchical microspheres.

Fig. 3 (a) Transmittance and (b) diffused reflectance spectra of films based on samples S1–S3 and nanoparticles with a similar thickness (4 ± 0.2 μm).

crystals grew larger, with a wide particle size distribution. In the ammonia solution, NH$_4^+$ was adsorbed on the nanoparticles' surface to enhance the interfacial surface tension for helping in crystal growth.

Fig. 2a displays that the TiO$_2$ hierarchical microsphere is relatively porous, while the nanoparticles in spheres interconnect tightly. Importantly, the connected nanopores emerged in the TiO$_2$ hierarchical spheres in the crystallization process (Fig. 2b). The pore size was feasibly tuned, depending on the ammonia concentration. After the hydrothermal treatment, the hierarchical microspheres grew into a highly crystalline anatase framework, which exhibited 0.35 nm spacing between adjacent layers, corresponding to the distance between (101) planes of the anatase structure (Fig. 2c). Fig. 2d also shows the X-ray diffraction (XRD) patterns of the samples (S1, S2 and S3), indicating that they have highly crystalline anatase structures without any impurity phase. Ammonia played an important role in the crystallization process of the TiO$_2$ hierarchical spheres, the crystallization of which was higher in the mixture solution with a higher ammonia concentration. The crystal sizes of the samples (S1, S2 and S3) determined from the full width at half maximum of the anatase (101) peak using the Scherrer equation were 7.40 nm, 13.12 nm and 15.30 nm, respectively, corresponding well to that measured from FE-SEM images.

In order to investigate the light characteristics of the TiO$_2$ hierarchical microsphere monolayer, the films with comparable thicknesses were prepared by the screen-printing technique. Typical films were prepared using *ca.* 20 nm anatase nanoparticles for comparison. Fig. 3 shows UV-vis transmittance and diffused reflectance spectra of films based on TiO$_2$ hierarchical microspheres and nanoparticles with a similar thickness (4 ± 0.2 μm). The nanoparticle film had a higher transmittance than 80% at the dye-sensitized wavelength range from 400 nm to 800 nm (Fig. 3a). However, the light in the S1 film was almost completely suppressed to transport through, in addition, the transmittance of the films based on samples S2
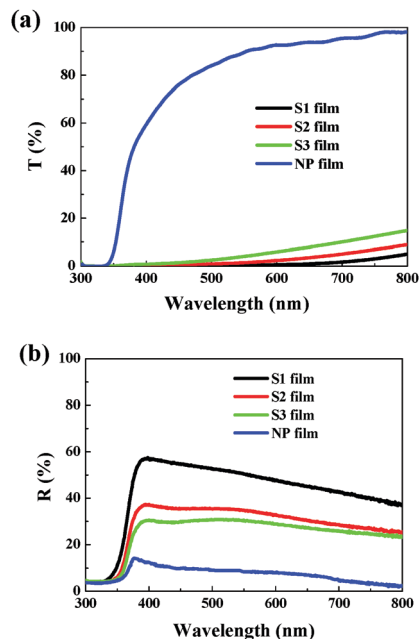
and S3 which were both less than 15%. Based on WGM, wavelength-scale dielectric spheres could diffractively couple light from free space as the photonic plasma to increase light adsorption.[26] The sub-wavelength diameters of the TiO$_2$ microspheres in 320–750 nm just corresponded to the dye sensitized light wavelength region so that the enhancement of light harvesting could lead to the increase of the charge injection efficiency. The diffused reflectance of TiO$_2$ hierarchical sphere films was much higher than that of nanoparticle films, indicating that TiO$_2$ hierarchical microspheres had a higher light scattering ability to scatter light many times for prolonging the optical path length in the films. The S1 film showed the strongest reflectance which was about 50% in the 400–800 nm range (Fig. 3b). The reflectance of S2 and S3 films was little lower than that of the S1 film due to larger pores in the S2 and S3 spheres, leading to more light transport through the spheres. In addition to enhancing the light harvesting, the films also had an ability to load enough dye molecules for light adsorption. Hence the adsorption capacity of the N719 dye was analysed by measuring the eluted dye concentration from the porous TiO$_2$ films using UV-vis absorption spectroscopy. Compared to 6.84×10^{-5} mol g^{-1} of the TiO$_2$ nanoparticles, the TiO$_2$ hierarchical microsphere films (S1, S2 and S3) displayed higher dye adsorption capacity values of 1.18×10^{-4}, 7.67×10^{-5} and 7.21×10^{-5} mol g^{-1}, respectively. The more the dye adsorption of the films, the larger the charge injection efficiency of DSCs. But the dye surface concentrations of TiO$_2$ hierarchical spheres were lower than 0.55 molecules per nm^2 of the nanoparticles, calculated from the BET specific surface area of the samples, whose concentrations were 0.47, 0.49 and 0.50 molecules per nm^2 for S1, S2 and S3 films. This result indicated that the surfaces inside the TiO$_2$ hierarchical spheres could be successfully

32296 | *Phys. Chem. Chem. Phys.,* 2016, **18**, 32293–32301

This journal is © the Owner Societies 2016

accessed to load by the dye molecules. The lower dye coverage of TiO₂ films leads to a positive shift of the conduction band and an increase of opportunities of charge recombination reaction with I₃⁻.[6,27]

To quantify the light utilization efficiency, the incident monochromatic photon-to-current conversion efficiencies (IPCEs) of DSCs based on the different hierarchical microspheres were measured, which were defined as the number of electrons flowing through the external circuit by an incident photon at a given wavelength. The IPCE can be rationalized using the following equation:[28]

$$IPCE(\lambda) = LHE(\lambda) \times \varphi_{inj} \times \eta_c \qquad (1)$$

where $LHE(\lambda)$ is the light harvesting efficiency, φ_{inj} is the quantum yield of the charge injection from the excited dyes to the TiO₂ conduction band, and η_c is the charge collection efficiency. The IPCE spectra of DSCs consisting of TiO₂ films sensitized with the N719 dye are shown in Fig. 4. The IPCE values of the TiO₂ hierarchical spheres were higher than those of the nanoparticles over the entire wavelength region, besides the IPCE spectra of S2 attained the highest value for which maximum value was 68.3% at 520 nm (Fig. 4a). By contrast the maximum IPCE of the nanoparticle film was only 52.2% at the same wavelength. Such a significant enhancement was likewise maintained in the red region of light (550–750 nm), for example, 54% IPCE at 600 nm for S2 films compared to 26.1% for nanoparticle films. Each IPCE maximum was normalized to 100% (Fig. 4b). It was visualized that the TiO₂ hierarchical sphere morphology had a strong impact on light

conversion efficiency, especially the conversion of lower photo energies at red light from 550 nm to 750 nm. We attributed the main factor to the enhancement of $LHE(\lambda)$ which is related to the dye uptake amount on the TiO₂ surface and light scattering. Much more effective light scattering and a larger adsorption amount of the N719 dye of TiO₂ hierarchical spheres would yield a larger $LHE(\lambda)$ value. This notable increase in IPCE would lead to a significant advantage in terms of short circuit current density (J_{sc}) for TiO₂ hierarchical sphere films. However, the IPCE values of the S1 films with the highest diffused reflectance and dye amount were lower than those of the S2 films. The S1 and S2 films had no difference in electron injection efficiency φ_{inj} with similar crystallinity, structure and dye, which was related to the energy discrepancy between the conduction band of TiO₂ and the excited level of the dye. So η_c was a critical factor affecting the light conversion efficiency of the TiO₂ hierarchical microsphere films. Two factors determined the charge collection efficiency, which also affected charge recombination at the TiO₂/electrolyte/dye surfaces and electron transport in the porous TiO₂ films.

The electron transport in mesoporous TiO₂ films of the DSCs has been interpreted by the multiple-trapping model,[29,30] which is limited by both trapping and the film morphology. The longer the charge transport pathway, the more the electrons undergo trapping and detrapping events and the longer they spend in the TiO₂ network before being collected by substrates. IMVS/IMPS was used to study the dynamics of electron recombination and transport in the films. IMPS and IMVS measurements were analysed to obtain the electron transport time (τ_d) and lifetime (τ_n) by fitting the frequency-dependent response using the expressions:[31]

$$\tau_d = 1/2\pi f_{dmin} \qquad (2)$$

$$\tau_n = 1/2\pi f_{nmin} \qquad (3)$$

where f_{dmin} is the characteristic frequency minimum of the IMPS imaginary component and f_{nmin} is the characteristic frequency minimum of the IMVS imaginary component. As shown in Fig. 5a, the electron transport times of DSCs as a function of the short circuit photocurrent (J_{sc}) under the 610 nm simulated light illumination were not seen to display a strong dependence relation. At the same photocurrent, DSC-S1 showed the longest electron transport time, in which τ_d values were about 2 times that of DSC-S2, whereas DSC-S3 and DCS-NP had the similar values. The electron transport time depended on not only the interparticle necking and the network topology of the TiO₂ films but also the light intensity and the distribution of traps.[32] For S1 hierarchical spheres with a well-defined structure, electron transport in the single sphere would be highly efficient, since the nanoparticles were tightly interconnected to one another with small pores. However, the neck area between the spheres was too small, which limited the electron transport resulting in the slow diffusion of electrons in S1 films. Another reason for the slow electron transport could be explained by the enlargement in the distribution of surface trap states in S1. The electron transport time involves an
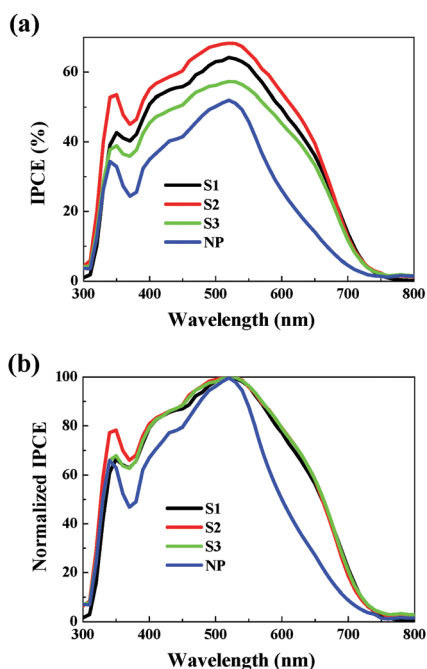

Fig. 4 (a) IPCE spectra of DSCs based on the 7.5 μm films composed of TiO₂ hierarchical spheres (S1, S2 and S3) or anatase nanoparticles with TiCl₄ post-treatment sensitized with the N719 dye, (b) the normalized IPCE spectra of DSCs.
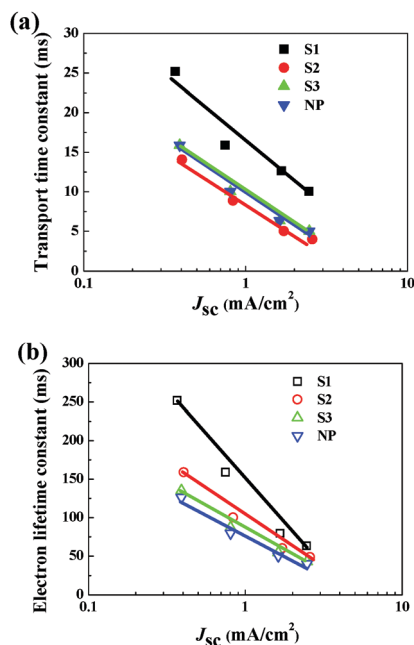
Fig. 5 Comparison of (a) electron transport time and (b) electron lifetime in the TiO$_2$ hierarchical spherical films and nanoparticle film as a function of the short circuit photocurrent for 610 nm laser illumination.

exponential distribution of the localized trap states, the dependence is expressed using the relation:[33]

$$\tau_d = J_{sc}^{\alpha-1} \qquad (4)$$

where parameter α is related to the steepness of the exponential trap-state distribution. The surface trap state is linearly proportional to the surface area of the inner film.[34] At the same short circuit photocurrent, the S1 film with a higher surface area had lower electron transport than those of the other samples. The spheres of S2 had a rather rough surface, and some amorphous sphere broke down to nanoparticles which would be placed in the voids between S2 hierarchical spheres to enlarge the neck area of the spheres. The structure based on this situation was beneficial for the electron diffusion, and especially the larger neck area allowed the large number of electrons to transfer, so the τ_d value of DCS-S2 was the smallest. However, the electrons did not transport fast in the single S3 sphere compared to the nanoparticle film because the nanoparticles of the S3 sphere with large size pores interconnect loosely. Furthermore, sample S3 had more amorphous spheres broke up into nanoparticles than sample S2 in the hydrothermal process so that the film prepared from S3 was similar to the nanoparticle films with large size pores and less coordination particles.

The electrons were dominantly captured by the surface-adsorbed molecular iodine species at the surface defect traps of the TiO$_2$ film. To account for recombination in the TiO$_2$ hierarchical microsphere film, the τ_n values of DSCs were evaluated by IMVS analysis as in Fig. 5b. The defect trap density of the TiO$_2$ hierarchical spheres with a larger surface area should be higher than that of the nanoparticles if we assumed that the surface defect trap density per unit area was the same,

which would result in an increase of the electron lifetime.[6,32] Fig. 5b shows clearly that the electron lifetimes of the TiO$_2$ hierarchical microspheres increase obviously with increasing BET surface areas. The τ_n value of DSC-S1 was observed to be superior, by about two times, in comparison to that of DSC-NP, indicating a slower electron recombination with the oxidized electrolyte species. But the relatively high value of the slope of the fitting line for DSC-S1 in Fig. 5b implies that the τ_n value reduces more rapidly with increasing short circuit photocurrent. The rate of recombination was in direct proportion to the electron concentration of the TiO$_2$ film, based on the transport-limited recombination model.[33] With an increase in the incident photon flux of 610 nm laser illumination, the electron injection efficiency of DSCs increased. The net increase in the number of injected charges of DSC-S1 with a larger amount of N719 dyes was larger than those of other DSCs. However, a larger number of charges were limited by the narrow neck between the individual spheres of the S1 film and could not be collected promptly by the substrate due to the slow electron transport in the S1 film. The accumulation of charges in the S1 film enhanced the electron concentration, more than those of other DSCs. So the rate of recombination of DSC-S1 increased more rapidly and the electron lifetime shortened more seriously.

The achievement of optimum η_c in the DSCs should require a faster electron transport and slower recombination between these two conflicting constraints. The charge collection efficiency of the photo-injected electrons from sensitized dyes was estimated from the respective time constants for the charge recombination and transport process, which is described using the relation:[35] $\eta_c = 1 - \tau_d/\tau_n$. The calculation shows that the charge collection efficiency of DSC-S2 was the highest, 91.80%, 5% improvement compared to that of DSC-NP. There was no discrepancy over the full range of the short circuit photocurrent for the η_c values in DSC-S2, DSC-S3 and DSC-NP. But the η_c value of DSC-S1 decreased from 90% at 0.37 mA cm^{-2} of the short circuit photocurrent to 84.15% at 2.46 mA cm^{-2}. The low charge collection efficiency led to a low IPCE value, which confirmed the IPCE analysis results.

To further understand the dynamics of electron transport and recombination in the DSCs, the EIS analysis of DSCs was conducted under forward bias (-0.76 V) in the dark. I$_3^-$ was generated at the counter electrode and penetrates the porous TiO$_2$ film by diffusion, and then was reduced at the TiO$_2$ surface traps by electrons transported through the TiO$_2$ film. The charge transfer resistance (R) and chemical capacitance (C) were obtained by fitting the semicircles in the Nyquist plots of Fig. 6. In the semicircles these internal resistances were related to the sheet resistance of substrates (R_1), the charge transfer processes at the Pt counter electrode (R_2), the charge transportation at the TiO$_2$/electrolyte/dye interfaces (R_3), and iodine Warburg diffusion in the electrolyte (R_{diff}), respectively. Here we focused on internal resistances at the TiO$_2$/electrolyte/dye interfaces and Warburg diffusion, in which the TiO$_2$ hierarchical microspheres played an important role in the long electron lifetime and fast iodine diffusion. It was obvious that the R_3 values of DSCs composed of TiO$_2$ hierarchical microspheres
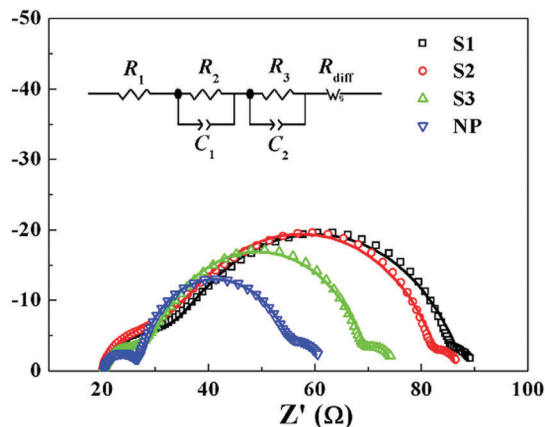
Fig. 6 Electrochemical impedance spectroscopy (Nyquist plots) of DSCs based on TiO_2 hierarchical spheres (S1, S2 and S3) and nanoparticles. The line in the figure shows the fitted results, the scattered dots are experimental data. The inset is the equivalent circuit.

were higher than that of DSC-NP, whereas the R_3 value decreased from 58.33 Ω of DSC-S1 to 40.96 Ω of DSC-S3 (Table 2). Strikingly, the electron recombination of DSC-S1 with higher resistance was more remarkably retarded. The capacitances increased linearly with the dye concentration of the samples from 0.75 mF of DSC-S1 to 0.92 mF of DSC-NP. The chemical capacitance was linearly dependent on the effective surface area which was coated by the dye.[36] The electron lifetime of DSCs could be calculated by $\tau_n = R_3 \times C_3$ from the EIS fitting results. The calculation revealed that DSCs based on TiO_2 hierarchical spheres had a longer electron lifetime compared to DSC-NP, corresponding to the IMVS analysis results. The diffusion of I^-/I_3^- redox couples in the TiO_2 film was dependent on the pore size and interconnection between the pores of the film. For the TiO_2 hierarchical microspheres, electrolyte diffusion in the individual internal spherical structure would not be efficient, since an internal pore diameter was rather small for highly efficient diffusion of electrolytes.[37] But the inefficient diffusion distance was very short in the spheres, such as only 360 nm of the maximum diffusion length from the surface to the core of the sphere with a diameter of 720 nm. However, the large external pores among the spheres of the TiO_2 film would provide a highway for electrolyte diffusion through the TiO_2 hierarchical sphere film. The Warburg resistances of DSCs based on the TiO_2 hierarchical spheres were much less than that of DSC-NP (Table 2), whereas the R_{diff} values increased from 1.29 Ω of DSC-S1 to 6.46 Ω of DSC-S2. The diffusion constants ($D_{I_3^-}$) of I_3^- ions were determined by fitting the impedance values to be higher than 3.46×10^{-6} cm² s⁻¹ of

DCS-NP (Table 2). A well-defined spherical film with a large pore structure between spheres was beneficial for electrolyte diffusion with a large diffusion constant, which would provide a higher short circuit photocurrent for DSCs.

The porous films were prepared from TiO_2 hierarchical microspheres as the photoelectrodes (7.5 ± 0.3 μm) to be assembled into the DSCs, and their reference cell (DSC-NP) was composed of 7.5 μm nanoparticles (around 20 nm) and 4 μm scattering layers of particles (diameter, around 300 nm), sensitized with the N719 dye. Fig. 7 shows the J–V characteristics of DSCs under simulated AM 1.5 sunlight (100 mW cm⁻²). Detailed photovoltaic parameters, such as the open-circuit voltage (V_{oc}), J_{sc}, the fill factor (FF), and the photovoltaic conversion efficiency (η), are summarized in Table 3. Comparing the performance of devices with different TiO_2 hierarchical microspheres, the V_{oc} value of DSC-S1 was the highest, 751 mV, whereas the V_{oc} values of the DSCs were observed to be reduced with decreasing BET surface areas of the samples. The Fermi energy level of the TiO_2 hierarchical microsphere film shifted negatively, originating from the enhancement of the electron concentration in the conduction band of films with increasing adsorbed dye amount. The fill factor was determined by the internal resistance of the DSCs. The FF values of DSCs prepared from the TiO_2 hierarchical spheres were higher than that of DSC-NP, due to these DSCs had smaller iodine Warburg resistances. Therefore, the major reason for the enhancement of the photovoltaic conversion efficiency was higher J_{sc} of DSCs due to more effective light scattering and larger surface areas for loading the dye molecules in the TiO_2 hierarchical

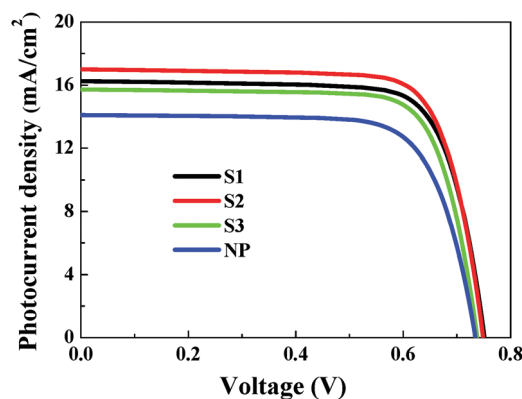**Fig. 7** J–V curves of DSCs prepared from the TiO_2 hierarchical microspheres and nanoparticle electrodes under simulated AM 1.5 sunlight (100 mW cm⁻²).

Table 2 The fitting data from the EIS measurements (Nyquist plots) of DSCs at −0.76 V forward bias in the dark

Samples	R_3 (Ohm)	C_3 (mF)	τ_{nEIS} (ms)	R_{diff} (Ohm)	$D_{I_3^-}$ (cm² s⁻¹)
S1	58.33	0.75	43.75	1.29	6.13×10^{-6}
S2	52.80	0.79	41.71	2.98	5.50×10^{-6}
S3	40.96	0.88	36.04	6.46	4.44×10^{-6}
NP	29.13	0.92	26.91	12.47	3.46×10^{-6}

Table 3 Photovoltaic properties of DSCs assembled by the electrodes of the TiO_2 hierarchical microspheres and nanoparticles with similar thicknesses

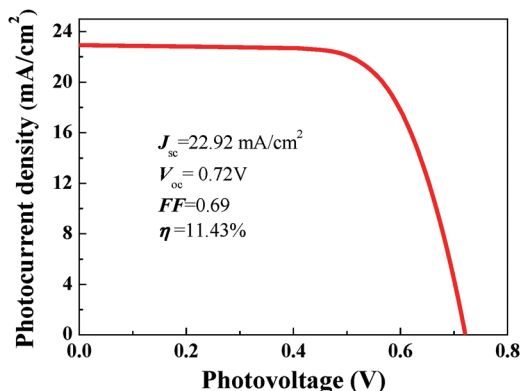| Samples	V_{oc} (mV)	J_{sc} (mA cm⁻²)	FF (%)	η (%)
S1	751	16.19	76.04	9.24 ± 0.13
S2	749	16.98	76.32	9.70 ± 0.12
S3	738	15.69	76.63	8.86 ± 0.22
NP	734	14.16	73.48	7.64 ± 0.23

Fig. 8 $J-V$ curves of DSC based on the S2 hierarchical microsphere electrodes sensitized by the C106 dye under simulated AM 1.5 sunlight (100 mW cm^{-2}).

microsphere films (Fig. 7). Notably, the DSCs composed of the microspheres exhibited higher J_{sc}, corresponding to the IPCE measurement results. The J_{sc} value of DSC-S2 showed 19.92% improvement from 14.16 mA cm^{-2} of DSC-NP. The TiO$_2$ hierarchical microspheres scattered the light many times in the film and loaded more dye molecules to adsorb the light, which aimed to take full advantage of light for DSCs. DSC-S2 exhibited the highest PCE of 9.70% with a V_{oc} of 749 mV, a J_{sc} of 16.98 mA cm^{-2}, and a FF of 76.32%, an 26.96% enhancement compared to 7.64% PCE of DSC-NP.

Furthermore, for yielding more high photovoltaic conversion efficiency, the S2 film was treated with TiCl$_4$ solution, and then sensitized by C106 dye molecules. The front of the solar cell was masked by an aperture, which was slightly larger than the TiO$_2$ area. Fig. 8 displays the high photovoltaic performance of DSCs based on the S2 film, exhibiting a PCE of 11.43%, with a V_{oc} of 720 mV, a J_{sc} of 22.92 mA cm^{-2}, and a FF of 69%. Thus, these results indicated that the DSCs fabricated using ultrathin porous monolayers based on the hierarchical microspheres exhibited a high efficiency, meanwhile, the lower amount of TiO$_2$ used cuts the cost of device manufacture.

4. Conclusions

In summary, highly crystalline TiO$_2$ hierarchical microspheres were prepared by hydrothermal treatment with various amounts of ammonia. These microspheres consisted of nanoparticles of various sizes, revealing a large surface area for dye adsorption and continuous pore distribution for electrolyte diffusion. The visible light through the TiO$_2$ hierarchical subwavelength microsphere film would be effectively scattered many times to enhance the light harvesting for DSCs, leading to higher IPCE values compared to that of DSC-NP in the 400–800 nm region. Strikingly, DSC-S2 collected electrons more efficiently with faster electron transport and longer lifetime, compared to DSC-NP. In addition, the electrolyte diffused easily through the large pore among the spheres. The DSCs based on the 7.5 μm TiO$_2$ hierarchical microspheres displayed excellent photovoltaic performances, besides DSC-S2 exhibiting the

highest conversion efficiency, 11.43%, significantly higher than 7.64% of DSC-NP. Therefore, the sub-wavelength microsphere could take full advantage of visible light in the ultrathin monolayer and loaded a large number of dyes for light adsorption. It was proven that the TiO$_2$ sub-wavelength microspheres were an excellent alternative for high efficiency and low cost DSCs.

Acknowledgements

Notes and references

1 M. Gratzel, *Acc. Chem. Res.*, 2009, **42**, 1788–1798.
2 N. G. Park, J. van de Lagemaat and A. J. Frank, *J. Phys. Chem. B*, 2000, **104**, 8989–8994.
3 B. Liu and E. S. Aydil, *J. Am. Chem. Soc.*, 2009, **131**, 3985–3990.
4 B. O. R. M. Gratzel, *Nature*, 1991, **353**, 737–740.
5 M. Koelsch, S. Cassaignon, J. F. Guillemoles and J. P. Jolivet, *Thin Solid Films*, 2002, **403–404**, 312–319.
6 J. Sheng, L. Hu, S. Xu, W. Liu, L. e. Mo, H. Tian and S. Dai, *J. Mater. Chem.*, 2011, **21**, 5457–5463.
7 T. B. V. Kai Zhu, N. R. Neale and A. J. Frank, *Nano Lett.*, 2007, **7**, 3739–3746.
8 J. Tian, Y. H. Leng, Z. H. Zhao, Y. Xia, Y. H. Sang, P. Hao, J. Zhan, M. C. Li and H. Liu, *Nano Energy*, 2015, **11**, 419–427.
9 X. W. Huang, P. Shen, X. M. Feng, Z. Tan, B. Zhao and S. T. Tan, *Nano*, 2012, **7**, 9.
10 H. Y. Chen, T. L. Zhang, J. Fan, D. B. Kuang and C. Y. Su, *ACS Appl. Mater. Interfaces*, 2013, **5**, 9205–9211.
11 S. H. A. Lee, N. M. Abrams, P. G. Hoertz, G. D. Barber, L. I. Halaoui and T. E. Mallouk, *J. Phys. Chem. B*, 2008, **112**, 14415–14421.
12 E. S. Kwak, W. Lee, N. G. Park, J. Kim and H. Lee, *Adv. Funct. Mater.*, 2009, **19**, 1093–1099.
13 E. Palomares, J. N. Clifford, S. A. Haque, T. Lutz and J. R. Durrant, *J. Am. Chem. Soc.*, 2003, **125**, 475–482.
14 I. S. Yang, J. S. You, S. D. Sung, C. W. Chung, J. Kim and W. I. Lee, *Nano Energy*, 2016, **20**, 272–282.
15 J. Ferber and J. Luther, *Sol. Energy Mater. Sol. Cells*, 1998, **54**, 265–275.
16 D. Chen, F. Huang, Y. B. Cheng and R. A. Caruso, *Adv. Mater.*, 2009, **21**, 2206–2210.
17 F. Huang, D. Chen, X. L. Zhang, R. A. Caruso and Y. B. Cheng, *Adv. Funct. Mater.*, 2010, **20**, 1301–1305.
18 Y. Ding, J. Sheng, Z. Yang, L. Jiang, L. E. Mo, L. Hu, Y. Que and S. Dai, *ChemSusChem*, 2016, **9**, 720–727.

19 Z. Q. Li, Y. P. Que, L. E. Mo, W. C. Chen, Y. Ding, Y. M. Ma, L. Jiang, L. H. Hu and S. Y. Dai, *ACS Appl. Mater. Interfaces*, 2015, **7**, 10928–10934.

20 D. P. Wu, Y. Wang, H. Dong, F. Zhu, S. Y. Gao, K. Jiang, L. M. Fu, J. P. Zhang and D. S. Xu, *Nanoscale*, 2013, **5**, 324–330.

21 L. H. Nguyen, H. K. Mulmudi, D. Sabba, S. A. Kulkarni, S. K. Batabyal, K. Nonomura, M. Gratzel and S. G. Mhaisalkar, *Phys. Chem. Chem. Phys.*, 2012, **14**, 16182–16186.

22 S. Eiden-Assmann, J. Widoniak and G. Maret, *Chem. Mater.*, 2003, **16**, 6–11.

23 S. D. Burnside, V. Shklover, C. Barbe, P. Comte, F. Arendse, K. Brooks and M. Gratzel, *Chem. Mater.*, 1998, **10**, 2419–2425.

24 Y. Song, S. N. Clafton, R. D. Pensack, T. W. Kee and G. D. Scholes, *Nat. Commun.*, 2014, **5**, 4933–4940.

25 K. Yan, Y. Qiu, W. Chen, M. Zhang and S. Yang, *Energy Environ. Sci.*, 2011, **4**, 2168–2176.

26 J. Grandidier, D. M. Callahan, J. N. Munday and H. A. Atwater, *Adv. Mater.*, 2011, **23**, 1272–1276.

27 G. Schlichthorl, S. Y. Huang, J. Sprague and A. J. Frank, *J. Phys. Chem. B*, 1997, **101**, 8141–8155.

28 L. Y. Liang, S. Y. Dai, L. H. Hu, F. T. Kong, W. W. Xu and K. J. Wang, *J. Phys. Chem. B*, 2006, **110**, 12404–12409.

29 J. Nelson, *Phys. Rev. B: Condens. Matter Mater. Phys.*, 1999, **59**, 15374–15380.

30 L. Peter, *J. Electroanal. Chem.*, 2007, **599**, 233–240.

31 J. van de Lagemaat, N. G. Park and A. J. Frank, *J. Phys. Chem. B*, 2000, **104**, 2044–2052.

32 A. J. Frank, N. Kopidakis and J. van de Lagemaat, *Coord. Chem. Rev.*, 2004, **248**, 1165–1179.

33 N. Kopidakis, K. D. Benkstein, J. van de Lagemaat and A. J. Frank, *J. Phys. Chem. B*, 2003, **107**, 11307–11315.

34 H. Wang, J. He, G. Boschloo, H. Lindstrom, A. Hagfeldt and S.-E. Lindquist, *J. Phys. Chem. B*, 2001, **105**, 2529–2533.

35 G. Schlichthorl, N. G. Park and A. J. Frank, *J. Phys. Chem. B*, 1999, **103**, 782–791.

36 A. Zaban, A. Meier and B. A. Gregg, *J. Phys. Chem. B*, 1997, **101**, 7985–7990.

37 Y. J. Kim, M. H. Lee, H. J. Kim, G. Lim, Y. S. Choi, N. G. Park, K. Kim and W. I. Lee, *Adv. Mater.*, 2009, **21**, 3668–3673.